JGR Space Physics

RESEARCH ARTICLE
10.1029/2025JA034766

**Key Points:**

- Using AAL-PIP data, we examined how AE, SYM-H, and solar wind dynamic pressure affect EMIC wave distribution in Earth's outer magnetosphere
- In the outer magnetosphere, during enhanced solar wind dynamic pressure or positive SYM-H, the MLT range covered by EMIC waves broadens
- As *L* increases, EMIC wave occurrence decreases for both bands, with H-band amplitude increasing and He-band amplitude decreasing

**Correspondence to:**
X. Gao and J. Sun,
gaoxl@ustc.edu.cn;
sunjicheng@pric.org.cn

**Citation:**
Shao, T., Gao, X., Sun, J., Lessard, M., Gauthier, C., & Lu, Q. (2026). The impact of geomagnetic indices and solar wind dynamic pressure on EMIC waves in Earth's outer magnetosphere: Observations from the AAL-PIP chain on the Antarctic. *Journal of Geophysical Research: Space Physics*, *131*, e2025JA034766. https://doi.org/10.1029/2025JA034766

Received 13 OCT 2025
Accepted 21 DEC 2025

# The Impact of Geomagnetic Indices and Solar Wind Dynamic Pressure on EMIC Waves in Earth's Outer Magnetosphere: Observations From the AAL-PIP Chain on the Antarctic

**Tong Shao[1,2,3], Xinliang Gao[1,2,3], Jicheng Sun[4], Marc Lessard[5], Chrystal Gauthier[5], and Quanming Lu[1,2,3]**

[1]CAS Key Laboratory of Geoscience Environment, School of Earth and Space Sciences, University of Science and Technology of China, Hefei, China, [2]CAS Center for Excellence in Comparative Planetology, Hefei, China, [3]Collaborative Innovation Center of Astronautical Science and Technology, Harbin, China, [4]Center for Space Physics and Astronomy, Polar Research Institute of China, Shanghai, China, [5]Space Science Center, University of New Hampshire, Durham, NH, USA

**Abstract** Electromagnetic ion cyclotron (EMIC) waves are a key driver of particle precipitation and energy redistribution in the magnetosphere. While they have been extensively studied in the inner magnetosphere, their behavior in the outer magnetosphere remains poorly understood. In this study, we utilize ground-based measurements from the Autonomous Adaptive Low-Power Instrument Platform (AAL-PIP) chain to investigate the occurrence and amplitude of H-band and He-band EMIC waves under varying AE, SYM-H, and solar wind dynamic pressure ($P_d$) in Earth's outer magnetosphere ($L > 7$). In the outer magnetosphere, both the occurrence rate and amplitude of EMIC waves increase under high AE and enhanced $P_d$ conditions, similar to responses in the inner magnetosphere. However, unlike the inner magnetosphere, where EMIC waves are generally confined near noon, enhanced $P_d$ in the outer magnetosphere drives waves across a broader magnetic local time (MLT) distribution, including the dawn and dusk sectors. Furthermore, during substorm periods, H-band EMIC waves are absent in the dawn sector—a feature rarely observed in the inner region. SYM-H shows only a weak correlation with wave amplitude and He-band wave occurrence, while a stronger correlation is found with H-band wave activity in both dawn and dusk sectors. Additionally, the radial dependencies also differ: as $L$ increases, the wave occurrence rate decreases for both bands, but H-band amplitudes increase while He-band amplitudes decrease. This likely reflects differences in ion composition and wave growth conditions at larger radial distances. This study provides new insights into the global distribution and driving physics of EMIC wave activity in the outer magnetosphere.

## 1. Introduction

Electromagnetic ion cyclotron (EMIC) waves are common electromagnetic emissions in the Earth's magnetosphere, typically occurring in the Pc1–Pc2 geomagnetic pulsation frequency range (Cornwall, 1965; Kennel & Petschek, 1966). EMIC waves play a significant role in regulating magnetospheric dynamics, including the precipitation of relativistic electrons (Blum et al., 2015; Drozdov et al., 2017; Gao et al., 2015; Ma et al., 2015; Usanova et al., 2014; Wang et al., 2014), the heating of heavy ions (Li et al., 2023; Yuan et al., 2016), and the loss of ring current ions ((Fuselier & Anderson, 1996; Thorne & Horne, 1994; Yuan et al., 2014). EMIC waves predominantly propagate quasi-parallel to the background magnetic field near the magnetic equator, with the wave normal angle increasing with magnetic latitude (Kang et al., 2021; Denton et al., 1992). Due to the presence of multiple ion species in the magnetosphere, EMIC waves are observed in three distinct frequency bands: H-band, He-band, and O-band, each occurring below the corresponding ion gyrofrequency (Denton, 2018; Denton et al., 2014; Hu et al., 2010).

The source regions of EMIC waves are typically confined within ±10° magnetic latitude around the magnetic equator (Allen et al., 2015; Keika et al., 2013; Kim et al., 2016; Min et al., 2012), and the waves are mainly excited by hot protons (10–100 keV) with temperature anisotropy (Huang et al., 2021; Kang et al., 2021; Yu & Yuan, 2019). Theoretical and observational studies indicate two primary excitation mechanisms for EMIC waves in Earth's magnetosphere: (a) ion injections from the plasma sheet during substorm activity, and (b) adiabatic compression caused by enhancement of solar wind dynamic pressure (Chen et al., 2020; Cornwall &

Schulz, 1971; Engebretson et al., 2018; McCollough et al., 2012; Wang et al., 2014; Xue et al., 2021, 2022). Consequently, the occurrence and spatial distribution of EMIC waves are strongly modulated by both solar wind dynamic pressure and geomagnetic indices. Based on THEMIS observations, Usanova et al. (2012) reported a significant increase in the occurrence rate of EMIC waves (0.1–5 Hz) from the noon to dusk sector during periods of enhanced AE index. Moreover, solar wind dynamic pressure enhancements can excite EMIC wave activity across the entire dayside. Using Van Allen Probe data, Chen et al. (2020) investigated the individual effects of solar wind pressure and substorm injections, concluding that AE index enhancements mainly intensify EMIC wave occurrence and amplitude on the dusk side, while dynamic pressure increases exert a stronger influence on the dayside. Furthermore, Jun et al. (2021), using coordinated observations from the RBSP and Arase satellites, demonstrated that dusk-side He-band EMIC waves in the inner magnetosphere are predominantly driven by substorm injections, whereas H-band waves near noon are primarily excited by solar wind dynamic pressure enhancements.

While EMIC waves have been frequently observed in the inner magnetosphere, recent satellite observations confirm their presence in the outer magnetosphere (Ni et al., 2015; Yu et al., 2017; Zhang et al., 2017). However, earlier studies primarily concentrated on the inner region ($L < \sim 8$), leaving EMIC waves in the outer magnetosphere relatively unexplored. Ground-based stations at high-latitude polar regions provide broad $L$-shell coverage and long-term continuous measurements, offering a valuable opportunity to study EMIC wave activity in the outer magnetosphere.

In this study, we use the data from the Autonomous Adaptive Low-Power Instrument Platform (AAL-PIP) chain on the Antarctic (Xu et al., 2019) during 2017–2022 to statistically analyze the global distribution of H-band and He-band EMIC waves in the outer magnetosphere. We further investigate the influence of the solar wind dynamic pressure, AE index, and SYM-H index on their global distributions. The paper is organized as follows: Section 2 describes the data sets and instrumentation; Section 3 outlines the wave selection methodology; Section 4 presents the statistical results; and Section 5 provides a summary and discussion of the findings.

## 2. Instrumentations and Data

The primary data set for this study was obtained from the AAL-PIP chain on the East Antarctic Plateau. This chain consists of six stations (PG0-PG5), covering the geomagnetic latitudes from 69.5° to 78.6°. The locations of these stations are shown in Figure 1. Each station is equipped with a search coil magnetometer that measures magnetic field data at a sampling rate of 10 Hz, recording the magnetic field components in two orthogonal directions: along the geomagnetic south ($B_x$) and along the geomagnetic east ($B_y$). To characterize the magnetic field topology, we calculated the $L$-shell ($L$) values at the magnetic equator corresponding to each station's location using the TS04 model (Tsyganenko & Sitnov, 2005) during geomagnetically quiet conditions. Among the six stations, PG0 and PG1 are frequently located beyond the magnetopause and thus lack consistent usable data. Consequently, our analysis focuses on data from stations PG2 to PG5, covering the years 2017–2022. Each column of Table 1 lists the geographic longitude, geographic latitude, magnetic longitude, magnetic latitude, and $L$ value for stations PG2 to PG5.

In addition, we also incorporate the geomagnetic substorm index (AE), storm index (SYM-H), and solar wind dynamic pressure ($P_d$). These parameters are obtained from the OMNI database with 1-min resolution (https://omniweb.gsfc.nasa.gov).

## 3. Wave Selection

To identify and distinguish EMIC wave events in different frequency bands, we applied the following selection criteria. (a) Wave events were classified based on their frequency range: H-band waves were identified between the equatorial proton gyrofrequency ($f_{cp}^{+}$) and helium ion gyrofrequency ($f_{cHe}^{+}$), and He-band waves were identified between $f_{cO}^{+}$ and $f_{cHe}^{+}$. O-band EMIC waves were excluded from this study due to strong influence of ULF waves. (b) To eliminate background noise, we only considered wave power spectral densities exceeding $10^{-4}$ nT$^2$/Hz. (c) A valid wave event was required to have a duration of at least 5 minutes. To minimize the influence of Earth's rotation on the observations, EMIC wave activity within each five-minute segment was treated as a distinct event. Due to the limitation of the AAL-PIP instruments, which record only two orthogonal components of the magnetic field, wave polarization information is not accessible. The ion gyrofrequencies used for band classification are

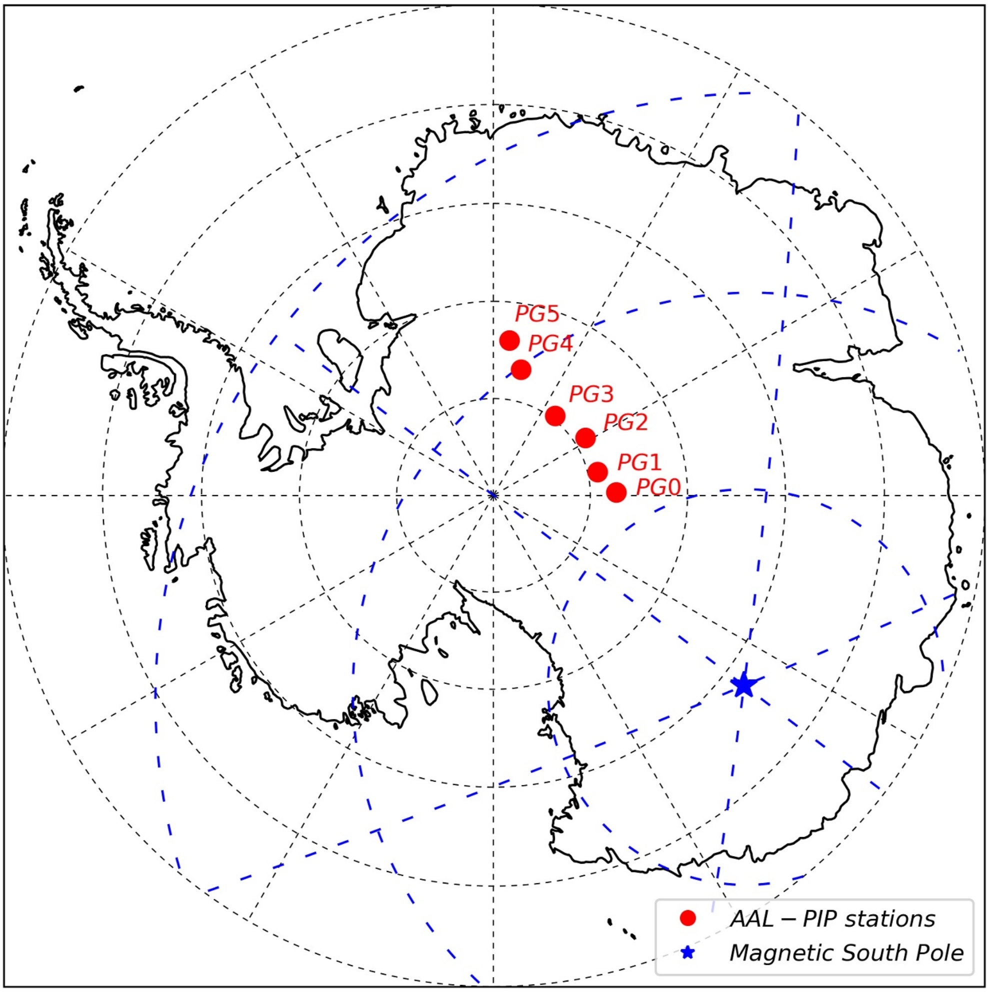

**Figure 1.** The locations of the AAL-PIP stations are marked with red dots.

calculated at the magnetic equator mapping to each ground station using the TS04 model. Since EMIC waves are typically generated near the magnetic equator and propagate to the ground stations, a time delay exists between wave generation and observation. In this study, we compute the propagation time by employing the cold plasma dispersion relation under the assumptions of a dipole magnetic field and parallel propagation along the field line. The number density along the path is specified using the model of Denton et al. (2002). At each spatial step ds, the group velocity $v_g$ is calculated and the corresponding time step is obtained as $\mathrm{dt} = \mathrm{ds}/\mathrm{v}_g$. Integrating dt from the magnetic equator to the ionospheric footprint along the field line yields the total propagation time. The results obtained using this method are consistent with those reported by Loto'aniu et al. (2005) when identical parameters are used. Additionally, time delays exist between the observations of EMIC waves and of the geomagnetic indices and solar wind conditions. We followed the estimation methods used by Usanova et al. (2012), Chen et al. (2020), and Jun et al. (2021) to determine the associated solar wind and geomagnetic parameters for each EMIC wave event. Specifically, the maximum solar wind dynamic pressure ($P_d$), the AE index and the SYM-H index were selected within the interval $[t_0 - 1\text{hour}, t_0 - 5\text{minutes}]$ for H-band waves, and within the interval $[t_0 - 1\text{hour}, t_0 - 2\text{minutes}]$ for He-band waves, where the different time intervals are chosen to account for the differing propagation times of H-band and He-band EMIC waves. Here, $t_0$ denotes the central time of the observed EMIC wave event.

**Table 1**
*The Coordinates of the AAL-PIP Stations*

| Station code | GeoLon | GeoLAT | MagLON | MagLAT | L |
|---|---|---|---|---|---|
| PG2 | 57.96 | −84.42 | 38.15 | 74.82 | 14.5 |
| PG3 | 37.63 | −84.81 | 37.09 | 73.54 | 12.5 |
| PG4 | 12.25 | −83.34 | 36.43 | 70.93 | 9.4 |
| PG5 | 5.71 | −81.96 | 37.12 | 69.49 | 8.1 |

## 4. Statistical Results

Figure 2 presents a representative set of EMIC wave events observed by multiple ground-based stations. Figures 2a–2c show the temporal variations of the solar wind dynamic pressure ($P_d$), AE index, and SYM-H index, respectively. In Figures 2a–2c, the black solid lines represent the time-shifted solar wind dynamic pressure and geomagnetic indices, while the orange dotted lines indicate the original OMNI measurements. As shown in Figures 2b and 2c, the AE index remains persistently below 100 nT, and the SYM-H index remains stable around zero, indicating the absence of intense substorm or storm activity. However, the solar wind dynamic pressure remains at a relatively high level around $P_d \approx 3$ nPa (Figure 2a), which contributes to the excitation of EMIC waves in the outer magnetosphere (Figures 2d–2g). Figures 2d–2g display the power spectral density (PSD) of magnetic field perturbations observed from station PG2 to PG5 derived via fast Fourier transform (FFT) at a frequency resolution of 0.025 Hz and a temporal resolution of 5 s. In these panels, the white solid, dashed, and dotted lines denote the equatorial proton, helium, and oxygen ion gyrofrequencies, respectively, calculated at the magnetic equator using the TS04 magnetic field model. Both H-band and He-band EMIC waves are observed across the stations, exhibiting distinct temporal and spatial characteristics. Specifically, H-band EMIC waves are first detected at the outermost station, PG2, followed sequentially by PG3 and PG4, suggesting a spatial response pattern to solar wind pressure enhancements. Figures 2h–2k illustrate the corresponding wave amplitudes. Here, black lines represent the amplitude of H-band EMIC waves, and blue lines represent the amplitude of He-band EMIC waves. The L-shell and magnetic local time (MLT) values listed at the bottom correspond to the station PG3, which moves from the dawn sector (MLT ≈ 3) to the dusk sector (MLT ≈ 21). Its *L*-shell variation is derived from mapping PG3 to the magnetospheric equatorial plane, which decreases from ∼16 in the dawn sector to a minimum of ∼10 near the noon sector, and then increases to ∼16 in the dusk side due to its longitudinal motion. Other stations follow similar *L*-shell and MLT evolution trends. Overall, the H-band wave amplitude decreases with decreasing $L$, from a peak value of ∼0.1 nT at PG2 to ∼0.06 nT at the inner stations. In contrast, the He-band EMIC waves do not show significant time lags across the different stations. Notably, their peak amplitudes exhibit the opposite $L$ dependence: the wave amplitude increases with decreasing $L$. This behavior may indicate that it is more favorable for the growth of He-band EMIC waves in the inner magnetosphere with stronger magnetic fields and higher $He^+$ densities (Kim et al., 2016).

Solar wind dynamic pressure ($P_d$) is a key driver of EMIC wave excitation in the magnetosphere. Figure 3 presents the *L*-MLT distribution of occurrence rates for H-band (a–d) and He-band (e–h) EMIC waves under four categories of solar wind dynamic pressure: $P_d \leq 1nPa$, $1nPa < P_d \leq 2nPa$, $2nPa < P_d \leq 3nPa$,and $P_d > 3nPa$. The magenta dashed contour denotes the average magnetopause positions for each pressure level (Shue et al., 1998). In this article, the colorbars for both occurrence rate and amplitude are plotted on a logarithmic scale. Under low pressure conditions ($P_d \leq 1nPa$), H-band EMIC waves exhibit the low occurrence rate (<10%), primarily distributed between 7 and 17 MLT. As $P_d$ increases beyond 2 nPa, the occurrence rate significantly increases, especially in the dawn (3–7 MLT) and dusk (15–21 MLT) sectors, reaching up to ∼30%. A similar trend is observed for He-band EMIC waves, whose occurrence expands from the noon sector (9–15 MLT) to a broader sector (6–18 MLT) as $P_d > 3nPa$, with occurrence rates exceeding 20%. Noticeably, the absence of data in the night sector (MLT ∼21–3) is due to the difficulties in mapping L-shell values in that region.

Figure 4 presents the corresponding average amplitudes. For H-band EMIC waves (a–d), amplitudes are minimal (∼0.01 nT) during quiet solar wind conditions but increase markedly with higher $P_d$, peaking near the noon sector at $L \sim 11$, reaching up to ∼0.1 nT. He-band waves (e–h) also exhibit amplification with increasing $P_d$, reaching peak values at $L = 6$–7 within 6–18 MLT. To study the L-shell dependence in detail, Figure 5 shows the noon sector (9–15 MLT) variation in occurrence rates (a–d) and amplitudes (e–h). H-band waves are most frequently observed at $L = 7$–8 under elevated dynamic pressure, while their amplitudes continue to increase toward higher $L$, peaking at $L > 10$ for $P_d > 3nPa$. In contrast, He-band wave amplitudes decrease with $L$, with the strongest wave activity confined to $L = 6$–7. Nevertheless, under high dynamic pressure, significant amplitudes also emerge at $L \approx 11$, potentially associated with wave generation near the magnetic field minima at higher latitudes. He-band waves have a distribution of occurrence similar to H-band waves.

The AE index serves as an indicator of substorm-induced ion injections, representing another important driver of EMIC wave activity. Figure 6 illustrates the L–MLT distribution of occurrence rates for H-band (a–c) and He-band (d–f) waves under three AE levels: AE ≤ 100nT, 100nT < AE ≤ 300nT, and AE > 300nT. Magnetopause locations corresponding to each AE level are shown in magenta dashed lines. Under quiet geomagnetic conditions

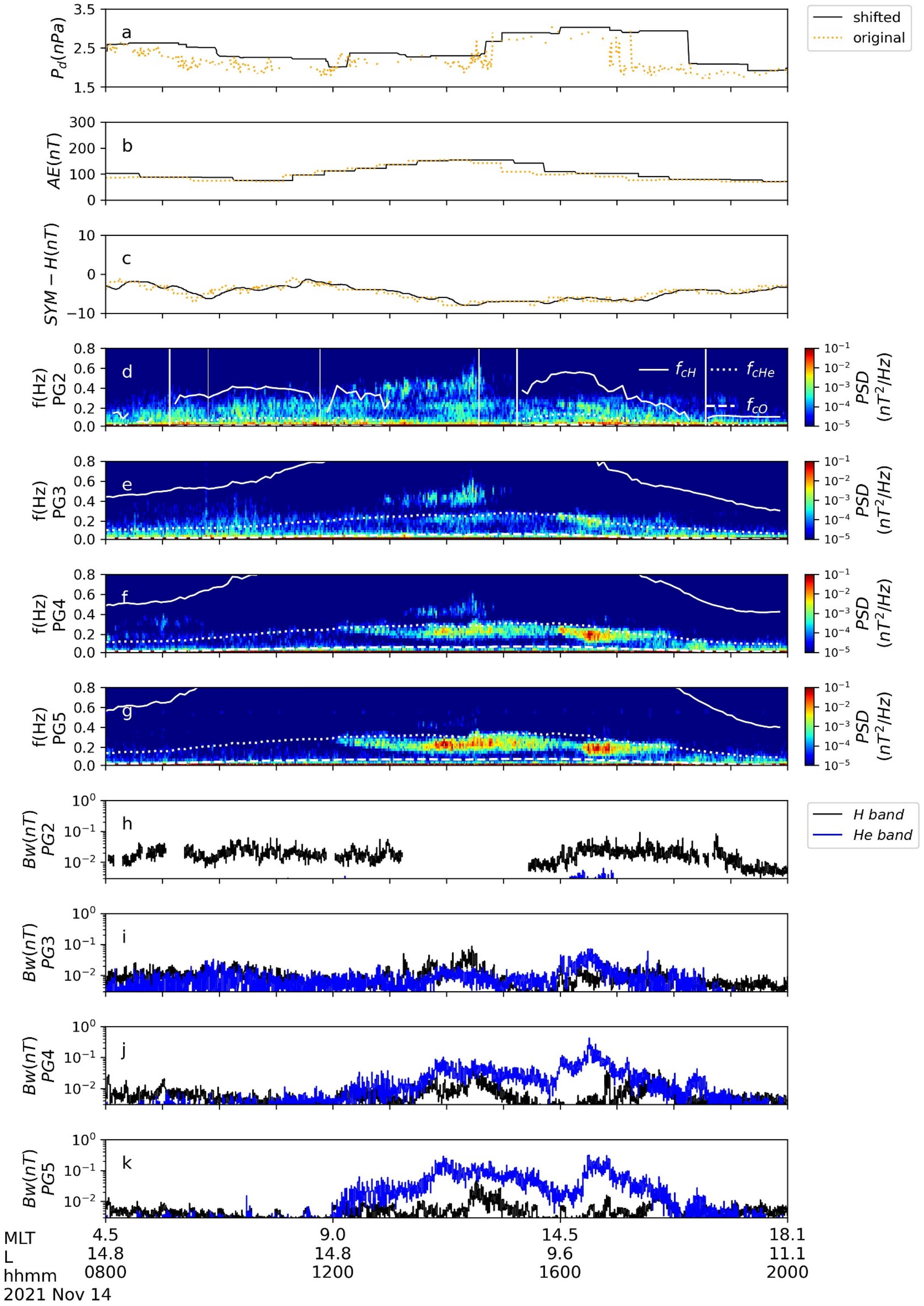

**Figure 2.** Observations on 14 November 2021. (a) Solar wind dynamic pressure. (b) AE Index. (c) SYM-H Index. (d–g) The temporal evolution of power spectrum density (PSD) of the total wave power of the magnetic field from search-coil magnetometer of ground sites PG2—PG5. (h–k) The amplitude of EMIC waves calculated from (d–g), where black lines represent the amplitude of H-band EMIC waves, and blue lines represent the amplitude of He-band EMIC waves.

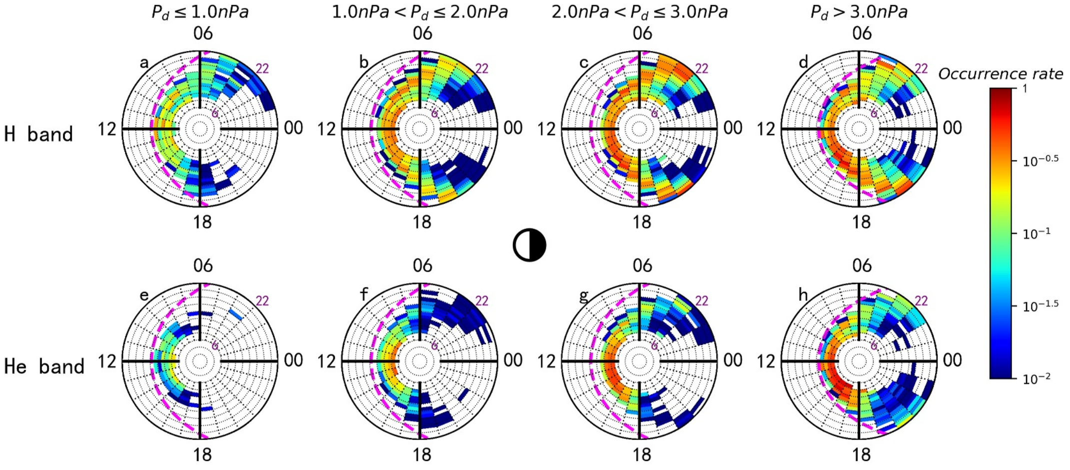

**Figure 3.** The distribution of wave occurrence rate in $L$-MLT planes of (a–d) H-band and (e–h) He-band EMIC waves for multiple intervals of solar wind dynamic pressure: (a, e) $P_d \leq 1nPa$, (b, f) $1nPa < P_d \leq 2nPa$, (c, g) $2nPa < P_d \leq 3nPa$, and (d, h) $P_d > 3nPa$.

(AE ≤ 100nT), H-band EMIC waves occur across 3–20 MLT with moderate rates (∼10%). As AE increases, enhanced wave occurrence is predominantly observed in the dusk sectors (17–21 MLT), with the occurrence rates rising from ∼15% to ∼30%. In contrast, the dawn sector (4–9 MLT) shows a decline in occurrence with increasing AE, dropping below 10% during active periods. Besides, occurrence rates in the post-midnight sector are consistently higher than those in the pre-midnight sector. He-band EMIC waves display a more confined MLT range but follow a similar AE dependent pattern: occurrence rates exceed 30% in the dayside region ($L$ < 10) during weak substorms, while expanding toward the dusk sector (up to 20 MLT) under high AE.

Figure 7 shows corresponding amplitude variations. Under quiet conditions, H-band amplitudes (a–c) remained moderate (∼0.02 nT on average). As AE increases, they roughly double in the noon to dusk sectors (10–21 MLT), and noticeable enhancements are also observed in the post-midnight region. He-band wave amplitudes (d–f) also intensify with AE, peaking at $L = 6$–7 within 9–17 MLT. Notably, both bands exhibit amplitude enhancements by a factor of ∼4 in the dawn sector (3–7 MLT) under active conditions.

Figure 8 further quantifies the L-shell dependence within the 10–17 MLT range. H-band wave occurrence rates (a–c) peak at $L = 6$–7 and decrease with increasing $L$. Under strong AE conditions, amplitudes notably increase at

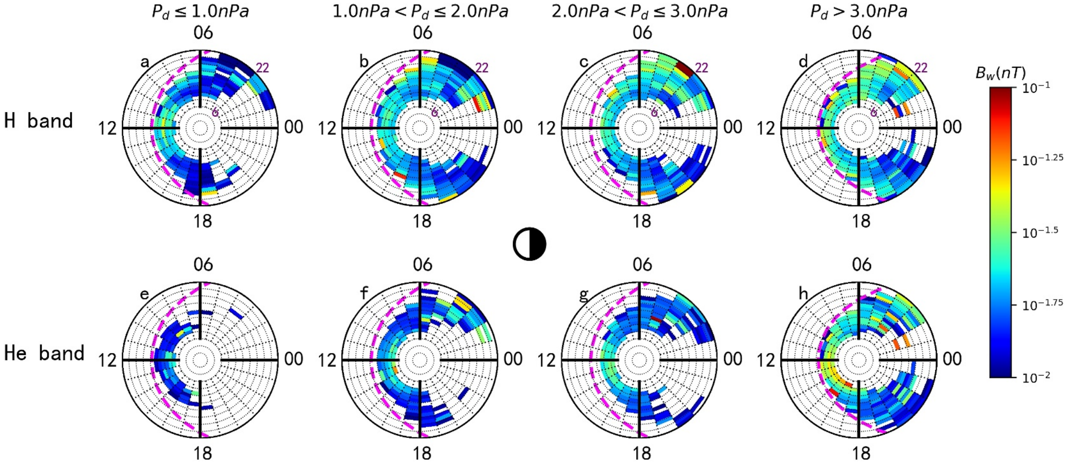

**Figure 4.** The distribution of wave amplitude in $L$-MLT planes of (a–d) H-band and (e–h) He-band EMIC waves for multiple intervals of solar wind dynamic pressure: (a, e) $P_d \leq 1nPa$, (b, f) $1nPa < P_d \leq 2nPa$, (c, g) $2nPa < P_d \leq 3nPa$, and (d, h) $P_d > 3nPa$.

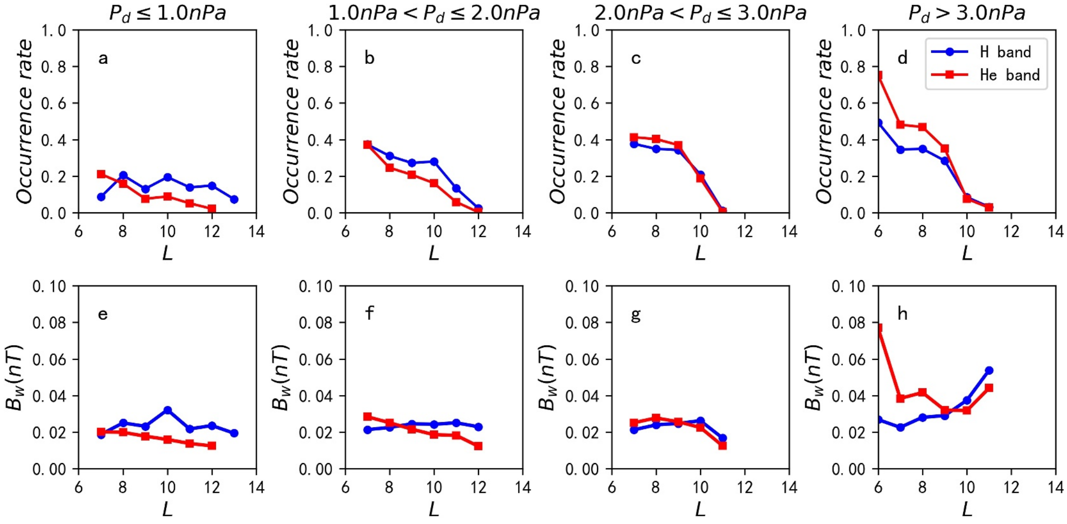

**Figure 5.** The distribution of wave (a–d) occurrence rate and (e–h) amplitude as a function of $L$ for H-band (blue bar) and He-band (red bar) EMIC waves for multiple intervals of solar wind dynamic pressure: (a, e) $P_d \le 1nPa$, (b, f) $1nPa < P_d \le 2nPa$, (c, g) $2nPa < P_d \le 3nPa$, and (d, h) $P_d > 3\ nPa$.

$L$ = 11–12. He-band waves (e–g) exhibit similar occurrence distributions, but their amplitudes consistently decline with increasing $L$, with a maximum at $L = 6$ regardless of AE intensity.

The SYM-H index, indicative of the geomagnetic storm activity, also influences the spatial distribution of EMIC waves. Figure 9 presents the $L$–MLT occurrence rates of H-band (a–d) and He-band (e–h) EMIC waves in four SYM-H categories: $\mathrm{SYM}-\mathrm{H} \le -20\mathrm{nT}$, $-20\mathrm{nT} < \mathrm{SYM}-\mathrm{H} \le -10\mathrm{nT}$, $-10\mathrm{nT} < \mathrm{SYM}-\mathrm{H} \le 10\mathrm{nT}$, and $\mathrm{SYM}-\mathrm{H} > 10\mathrm{nT}$. When $\mathrm{SYM}-\mathrm{H} \le -20\mathrm{nT}$, H-band EMIC waves are concentrated between 9 and 19 MLT, with occurrence rate exceeding 20%. As SYM-H increases, wave occurrence shifts toward the dawn sector (4–8 MLT), increasing from ∼10% to ∼30%, while occurrence in the dusk and noon sectors remains relatively stable. Under compressed magnetospheric conditions ($\mathrm{SYM}-\mathrm{H} > 10\mathrm{nT}$), H-band EMIC waves span 3–21 MLT, with the dayside occurrence consistently exceeding 30%. He-band EMIC waves maintain a stable distribution between 9 and 17 MLT for $\mathrm{SYM}-\mathrm{H} \le 10\mathrm{nT}$ but exhibit enhanced occurrence near the dawn (∼6 MLT) and dusk (∼18 MLT) sector at $L \approx 6$–7 under $\mathrm{SYM}-\mathrm{H} > 10\mathrm{nT}$.

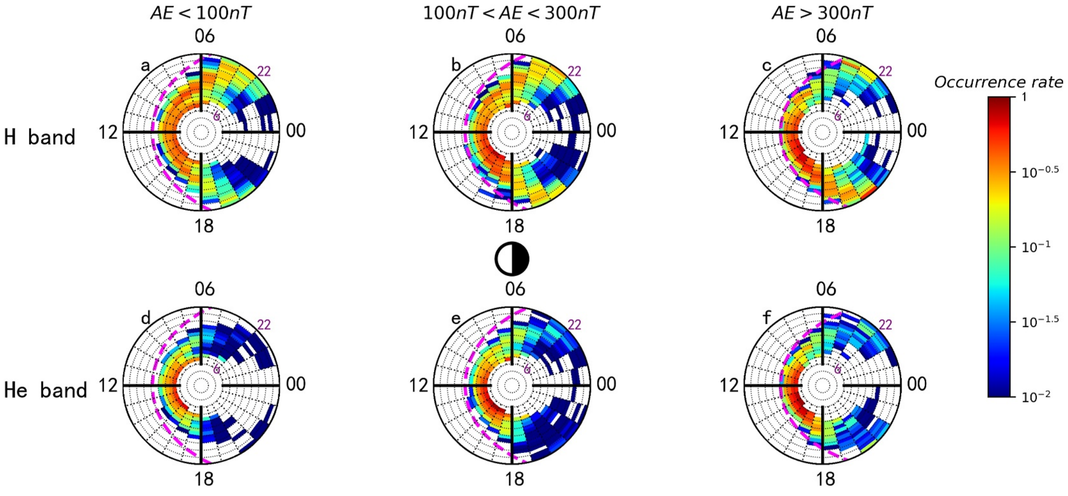

**Figure 6.** The distribution of wave occurrence rate in $L$-MLT planes of (a–c) H-band and (d–f) He-band EMIC waves for multiple intervals of AE: (a, d) $\mathrm{AE} \le 100\mathrm{nT}$, (b, e) $100\mathrm{nT} < \mathrm{AE} \le 300\mathrm{nT}$, (c, f) and $\mathrm{AE} > 300\mathrm{nT}$.

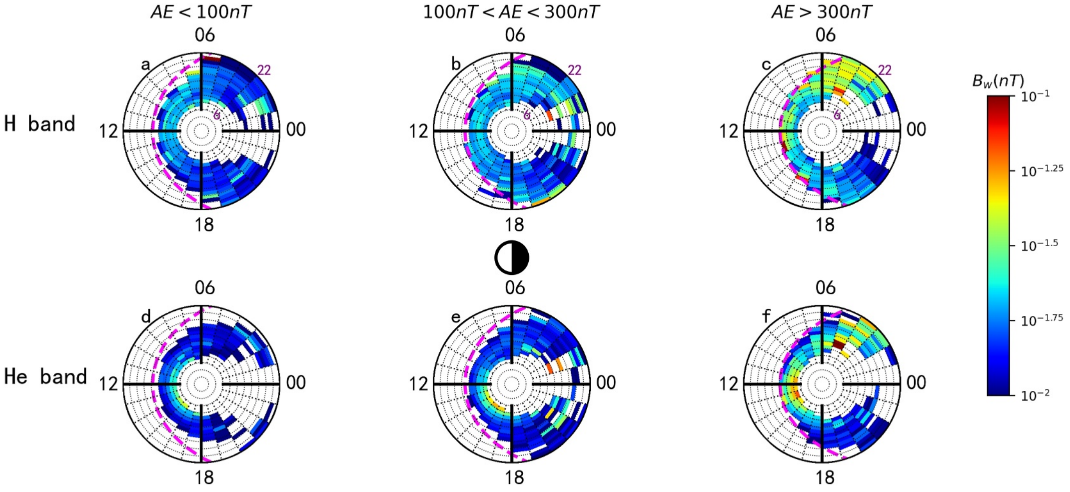

**Figure 7.** The distribution of wave amplitude in *L*-MLT planes of (a–c) H-band and (d–f) He-band EMIC waves for multiple intervals of AE: (a, d) AE ≤ 100nT, (b, e) 100nT < AE ≤ 300nT, (c, f) and AE > 300nT.

Figure 10 presents average wave amplitudes under the same SYM-H intervals. H-band wave amplitudes (a–d) show minor enhancement in the noon to afternoon sectors during $\mathrm{SYM} - \mathrm{H} \le -20\mathrm{nT}$, but remain low (~0.01 nT) during quiet periods. Under compressed conditions ($\mathrm{SYM} - \mathrm{H} > 10\mathrm{nT}$), amplitudes increase within 10–16 MLT, reaching up to ~0.03 nT. He-band wave amplitudes (e–h) are generally weak under quiet conditions but increase significantly under storm and compressed magnetospheric conditions, particularly within 6–18 MLT. Figure 11 further highlights the *L*-shell dependence within 9–17 MLT. The occurrence of H-band EMIC waves (a–d) peaks at $L = 6$–7 and declines with increasing *L*. During periods of $\mathrm{SYM} - \mathrm{H} \le -20\mathrm{nT}$ and $\mathrm{SYM} - \mathrm{H} > 10\mathrm{nT}$, their amplitudes increase with *L*, suggesting enhanced wave growth in the outer magnetosphere. Similar to the H-band, the occurrence rate of He-band also declines with increasing *L*. In contrast, amplitudes of He-band waves (e–h) decrease monotonically with *L*, peaking consistently at $L \approx 6$ across all SYM-H conditions.

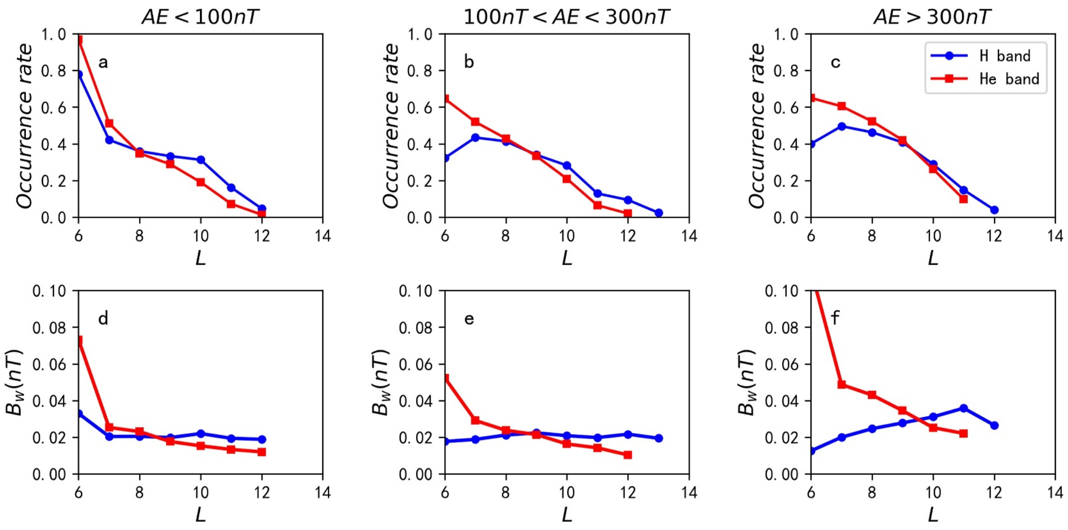

**Figure 8.** The distribution of wave (a–c) occurrence rate and (d–f) amplitude as a function of *L* for H-band (blue bar) and He-band (red bar) EMIC waves for multiple intervals of AE: (a, d) AE ≤ 100nT, (b, e) 100nT < AE ≤ 300nT, (c, f) and AE > 300nT.

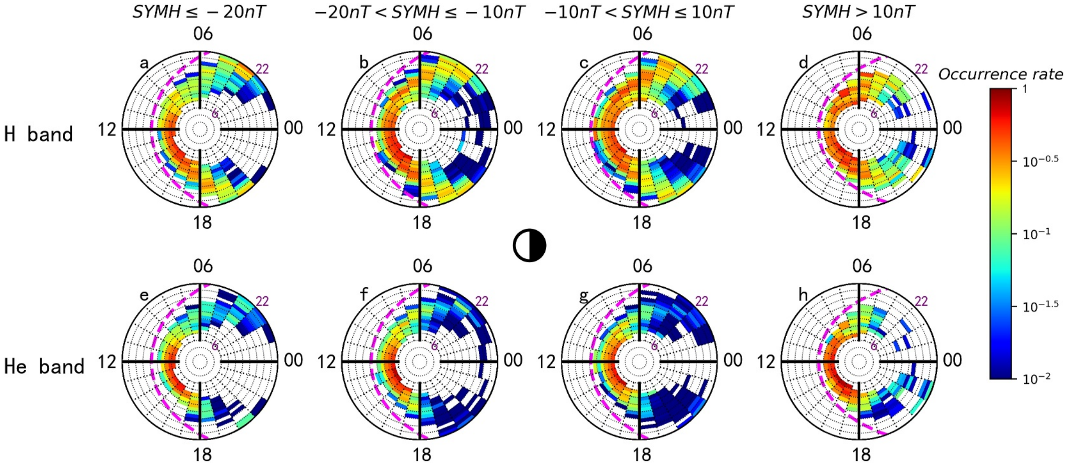

**Figure 9.** The distribution of wave occurrence rate in L-MLT planes of (a–d) H-band and (e–h) He-band EMIC waves for multiple intervals of SYM-H: (a, e) $\text{SYMH} \le -20nT$, (b, f) $-20\text{nT} < \text{SYM} - \text{H} \le -10nT$, (c, g) $-10\text{nT} < \text{SYM} - \text{H} \le 10\text{nT}$, and (d, h) $\text{SYM} - \text{H} > 10nT$.

## 5. Discussion and Conclusions

In this paper, we use observations from ground-based stations in the AAL-PIP chain to investigate the dependence of EMIC waves on AE, SYM-H and solar wind dynamic pressure in the Earth's outer magnetosphere. Our principal findings are summarized as follows:

1. With increasing dynamic pressure, both the occurrence rate and amplitude of EMIC waves increase, and their MLT coverage broadens, particularly at the dawn and dusk sectors.
2. As AE increases, the occurrence rate and amplitude of EMIC waves enhance from noon to the afternoon sector, while H-band EMIC waves diminish in the dawn sector.
3. The SYM-H index exerts minimal influence on the occurrence rate of EMIC waves overall; however, H-band EMIC waves occur more frequently in the dawn sector during periods of negative SYM-H.
4. EMIC wave occurrence decreases with increasing *L* in the outer-magnetosphere. The amplitude of He-band EMIC waves decreased with increasing *L*, while H-band waves exhibited a broader *L*-shell distribution.

Our results provide several new insights into the properties of EMIC waves in the outer magnetosphere. First, the strong dependence on solar wind dynamic pressure highlights the importance of magnetospheric compression in

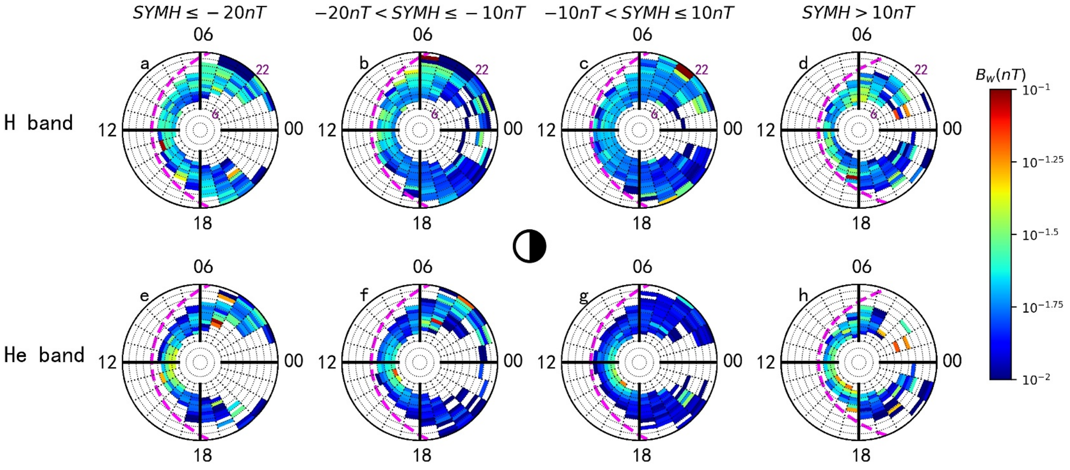

**Figure 10.** The distribution of wave amplitude in *L*-MLT planes of (a–d) H-band and (e–h) He-band EMIC waves for multiple intervals of SYM-H: (a, e) $\text{SYMH} \le -20nT$, (b, f) $-20\text{nT} < \text{SYM} - \text{H} \le -10nT$, (c, g) $-10\text{nT} < \text{SYM} - \text{H} \le 10\text{nT}$, and (d, h) $\text{SYM} - \text{H} > 10nT$.

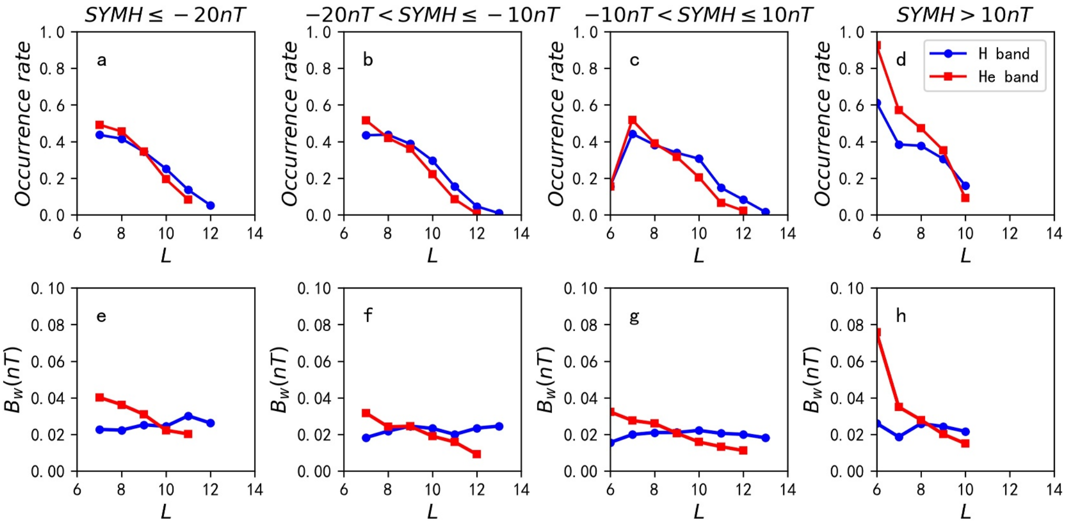

**Figure 11.** The relevant to this study. distribution of wave (a–d) occurrence rate and (e–h) amplitude as a function of L for H-band (blue bar) and He-band (red bar) EMIC waves for multiple intervals of SYM-H: (a, e) $\mathrm{SYM}-\mathrm{H}\leq -20nT$, (b, f) $-20\mathrm{nT}<\mathrm{SYM}-\mathrm{H}\leq -10nT$, (c, g) $-10\mathrm{nT}<\mathrm{SYM}-\mathrm{H}\leq 10\mathrm{nT}$, and (d, h) $\mathrm{SYM}-\mathrm{H}>10nT$.

wave excitation. While earlier studies have shown that dynamic pressure primarily enhances EMIC waves in the noon sector within the inner magnetosphere (e.g., Meredith et al., 2014; Usanova et al., 2012), we find that the enhanced MLT coverage extends from 3 to 21 MLT under high $P_d$ in the outer magnetosphere. This indicates that solar wind compression has a more global impact in the outer regions, possibly due to the proximity of the magnetopause and stronger field-line stretching at large *L*.

Second, the AE dependence reveals that substorm-related ion injections also play a key role in wave growth. The enhanced occurrence in the dusk-to-afternoon sectors during active periods suggests a close link with substorm injection regions, consistent with results reported by Chen et al. (2020) in the inner magnetosphere. However, we also observe a decrease in dawnside occurrence for H-band waves when AE > 300 nT, which contrasts with the stronger dawnside activity sometimes found at lower L. This difference likely reflects a different source region of free energy for those EMIC waves. Jun et al. (2021) proposed that one possible candidate for a free energy source is the temperature anisotropy by low-energy protons in the warm plasma cloak (<1 keV) via $E \times B$ drift.

Third, the SYM-H index also modulates EMIC wave occurrence and amplitude. As SYM-H increases from negative to positive, the occurrence shifts toward the dawn sector, suggesting that cold plasma refilling and plasmaspheric plume formation may provide favorable conditions for dawnside H-band wave generation. Under conditions SYM-H > 10 nT, we found broad MLT coverage (3–21 MLT) with persistently high dayside occurrence (>30%). This is likely related to magnetopause compression. Thus, while SYM-H has only a modest effect on overall occurrence rates compared with dynamic pressure or AE, it controls the spatial redistribution of EMIC activity between the dawn and noon sectors and highlights the importance of magnetospheric compression in the outer regions.

Besides, compared with the inner magnetosphere with a strong inertial magnetic field, the enhanced occurrence of EMIC waves in the outer magnetosphere highlights their important role in the overall magnetospheric dynamics. In this region, the weaker background magnetic field and lower plasma density allow even modest solar wind compressions to significantly alter the local plasma environment, facilitating EMIC wave growth. The increased wave activity at higher L-shells suggests that these regions are particularly effective for resonant interactions with ring current and radiation belt particles. Such interactions can lead to efficient pitch-angle scattering and subsequent precipitation into the atmosphere, contributing to the loss of energetic particles during geomagnetic disturbances.

In addition, although H-band and He-band EMIC waves generally exhibit similar occurrence rate dependences, their amplitude dependences on *L* differ. He-band amplitudes decrease rapidly with *L*, remaining strongest at $L = 6$–7, whereas H-band waves extend to larger *L* and are enhanced near the magnetopause. This difference likely reflects the decreasing $He^+$ concentration at larger $L$-Shells. With increasing $L$, the total ion number density decreases, thereby reducing the growth rate of He-band EMIC waves. The enhancements of H-band EMIC waves near the magnetopause may be associated with the wave generation at the magnetic field local minimum.

In our statistical analysis, since there are only two orthogonal directions of magnetic field perturbations, other wave modes, such as fast magnetosonic waves, could in principle contribute to the observed perturbations; however, our wave selection is based primarily on the frequency range of the fluctuations. The events analyzed here fall neatly between the proton and heavy ion gyrofrequencies, which is consistent with the typical frequency domain of EMIC waves. Additionally, given that the ground-based data only provides two components of the magnetic field and wave damping during propagation, the resulting amplitude is lower than the actual value. O-band EMIC waves are excluded owing to significant modulation by ULF waves. Previous studies have shown that the occurrence rate and amplitude of O-band EMIC waves (Saikin et al., 2015) are much lower than H-band and He-band EMIC waves. Although the TS04 model is widely used to estimate L-shells, uncertainties remain in the L-shells of EMIC waves observed on the ground for two reasons: First, the projection of L-Shell values introduces inherent uncertainties due to the uncertain source region. Second, horizontal propagation of EMIC waves after reaching the ionosphere can further affect the observed locations. Moreover, the TS04 model has limitations on the nightside, particularly near midnight, which may lead to an underestimation of EMIC wave activity in this region. This limitation likely contributes to the lack of coverage in the night sector observed in the plots (e.g., Figures 3, 4, 6, 7, 9, and 10). Finally, ground-based observations do not provide direct measurements of plasma number density or magnetic latitude (MLAT), both of which are essential for fully understanding wave generation and propagation. Future studies incorporating both ground-based and satellite observations will be critical to address these limitations.

Compared with the inner magnetosphere, EMIC waves in the outer magnetosphere exhibit both similarities and notable differences in the spatial distribution and driving conditions. These findings suggest that integrating statistical results from both regions could enable the development of a more comprehensive wave model. Such a model would improve the accuracy of the whole magnetosphere forecasts by better capturing wave-particle interactions across a wider spatial domain.

## Conflict of Interest

The authors declare no conflicts of interest relevant to this study.

## Data Availability Statement

The data from OMNI are available at https://omniweb.gsfc.nasa.gov/. The station data from AAL-PIP are available at the website (http://mist.nianet.org/).

**Acknowledgments**
This work was supported by the National Key Research and Development Program of China (2023YFC2808905), the NSFC Grants 42322406, 42204169, and 42230201, National Key Research and Development Program of China (No. 2022YFA1604600), the "USTC Tang Scholar" program, and the Fundamental Research Funds for the Central Universities (KY2080000063 and KY2080000138), the U.S. National Science Foundation under NSF awards 1745041, 1744828, and 2027168.

## References

Allen, R., Zhang, J., Kistler, L., Spence, H., Lin, R., Klecker, B., et al. (2015). A statistical study of EMIC waves observed by cluster: 1. Wave properties. *Journal of Geophysical Research: Space Physics*, *120*(7), 5574–5592. https://doi.org/10.1002/2015JA021333

Blum, L. W., Halford, A., Millan, R., Bonnell, J. W., Goldstein, J., Usanova, M., et al. (2015). Observations of coincident EMIC wave activity and duskside energetic electron precipitation on 18-19 January 2013. *Geophysical Research Letters*, *42*(14), 5727–5735. https://doi.org/10.1002/2015GL065245

Chen, H., Gao, X., Lu, Q., Tsurutani, B. T., & Wang, S. (2020). Statistical evidence for EMIC wave excitation driven by substorm injection and enhanced solar wind pressure in the Earth's magnetosphere: Two different EMIC wave sources. *Geophysical Research Letters*, *47*(21), e2020GL090275. https://doi.org/10.1029/2020GL090275

Cornwall, J. M. (1965). Cyclotron instabilities and electromagnetic emissions in the ultra-low frequency and very low frequency ranges. *Journal of Geophysical Research*, *70*(1), 61–69. https://doi.org/10.1029/JZ070i001p00061

Cornwall, J. M., & Schulz, M. (1971). Electromagnetic ion-cyclotron instabilities in multicomponent magnetospheric plasmas. *Journal of Geophysical Research*, *76*(31), 7791–7796. https://doi.org/10.1029/JA076i031p07791

Denton, R. E. (2018). Electromagnetic ion cyclotron wavefields in a realistic dipole field. *Journal of Geophysical Research: Space Physics*, *123*(2), 1208–1223. https://doi.org/10.1002/2017JA024886

Denton, R. E., Goldstein, J., Menietti, J. D., & Young, S. L. (2002). Magnetospheric electron density model inferred from polar plasma wave data. *Journal of Geophysical Research*, *107*(A11), 1386. https://doi.org/10.1029/2001JA009136

Denton, R. E., Hudson, M. K., & Roth, I. (1992). Loss-cone-driven ion cyclotron waves in the magnetosphere. *Journal of Geophysical Research*, *97*(A8), 12093–12103. https://doi.org/10.1029/92JA00954

Denton, R. E., Jordanova, V. K., & Fraser, B. J. (2014). Effect of spatial density variation and O+ concentration on the growth and evolution of electromagnetic ion cyclotron waves. *Journal of Geophysical Research: Space Physics*, *119*(10), 8372–8395. https://doi.org/10.1002/2014JA020384

Drozdov, A. Y., Shprits, Y. Y., Usanova, M. E., Aseev, N. A., Kellerman, A. C., & Zhu, H. (2017). EMIC wave parameterization in the long-term VERB code simulation. *Journal of Geophysical Research*, *122*(8), 8488–8501. https://doi.org/10.1002/2017JA024389

Engebretson, M. J., Posch, J. L., Braun, D. J., Li, W., Ma, Q., Kellerman, A. C., et al. (2018). EMIC wave events during the four GEM QARBM challenge intervals. *Journal of Geophysical Research: Space Physics*, *123*(8), 6394–6423. https://doi.org/10.1029/2018JA025505

Fuselier, S. A., & Anderson, B. J. (1996). Low-energy He+ and H+ distributions and proton cyclotron waves in the afternoon equatorial magnetosphere. *Journal of Geophysical Research*, *101*(A6), 13255–13265. https://doi.org/10.1029/96JA00292

Gao, X., Li, W., Bortnik, J., Thorne, R. M., Lu, Q., Ma, Q., et al. (2015). The effect of different solar wind parameters upon significant relativistic electron flux dropouts in the magnetosphere. *Journal of Geophysical Research: Space Physics*, *120*(6), 4324–4337. https://doi.org/10.1002/2015JA021182

Hu, Y., Denton, R. E., & Johnson, J. R. (2010). Two-dimensional hybrid code simulation of electromagnetic ion cyclotron waves of multi-ion plasmas in a dipole magnetic field. *Journal of Geophysical Research*, *115*(A9), A09218. https://doi.org/10.1029/2009JA015158

Huang, Z., Yuan, Z., Yu, X., Xue, Z., & Ouyang, Z. (2021). Simultaneous generation of EMIC and MS waves during the magnetic dip in the inner magnetosphere. *Geophysical Research Letters*, *48*(18), e2021GL094842. https://doi.org/10.1029/2021GL094842

Jun, C.-W., Miyoshi, Y., Kurita, S., Yue, C., Bortnik, J., Lyons, L., et al. (2021). The characteristics of EMIC waves in the magnetosphere based on the Van Allen Probes and Arase observations. *Journal of Geophysical Research: Space Physics*, *126*(6), e2020JA029001. https://doi.org/10.1029/2020JA029001

Kang, N., Lu, Q., Gao, X., Wang, X., Chen, H., & Wang, S. (2021). Propagation of electromagnetic ion cyclotron waves in a dipole magnetic field: A 2-D hybrid simulation. *Journal of Geophysical Research: Space Physics*, *126*(12), e2021JA029720. https://doi.org/10.1029/2021JA029720

Keika, K., Takahashi, K., Ukhorskiy, A. Y., & Miyoshi, Y. (2013). Global characteristics of electromagnetic ion cyclotron waves: Occurrence rate and its storm dependence. *Journal of Geophysical Research: Space Physics*, *118*(7), 4135–4150. https://doi.org/10.1002/jgra.50385

Kennel, C. F., & Petschek, H. E. (1966). Limit on stably trapped particle fluxes. *Journal of Geophysical Research*, *71*(1), 1–28. https://doi.org/10.1029/JZ071i001p00001

Kim, K.-H., Park, J., Omura, Y., Shiokawa, K., Lee, D., Kim, G., et al. (2016). Spectral characteristics of steady quiet-time EMIC waves observed at geosynchronous orbit. *Journal of Geophysical Research: Space Physics*, *121*(9), 8640–8660. https://doi.org/10.1002/2016JA022957

Li, X., Wang, R., Gao, X., Lu, Q., Chen, H., & Ma, J. (2023). Observation of non-resonance interactions between cold protons and EMIC waves of different polarizations in the inner magnetosphere. *Geophysical Research Letters*, *50*(23), e2023GL104431. https://doi.org/10.1029/2023GL104431

Loto'aniu, T. M., Fraser, B. J., & Waters, C. L. (2005). Propagation of electromagnetic ion cyclotron wave energy in the magnetosphere. *Journal of Geophysical Research*, *110*(A7), A07214. https://doi.org/10.1029/2004JA010816

Ma, Q., Li, W., Thorne, R. M., Ni, B., Kletzing, C. A., Kurth, W. S., et al. (2015). Modeling inward diffusion and slow decay of energetic electrons in the Earth's outer radiation belt. *Geophysical Research Letters*, *42*(4), 987–995. https://doi.org/10.1002/2014GL062977

McCollough, J. P., Elkington, S. R., & Baker, D. N. (2012). The role of Shabansky orbits in compression-related electromagnetic ion cyclotron wave growth. *Journal of Geophysical Research*, *117*(A1), A01208. https://doi.org/10.1029/2011JA016948

Meredith, N. P., Horne, R. B., Kersten, T., Fraser, B. J., & Grew, R. S. (2014). Global morphology and spectral properties of EMIC waves derived from CRRES observations. *Journal of Geophysical Research: Space Physics*, *119*(7), 5328–5342. https://doi.org/10.1002/2014JA020064

Min, K., Lee, J., Keika, K., & Li, W. (2012). Global distribution of EMIC waves derived from THEMIS observations. *Journal of Geophysical Research*, *117*(A5), A05219. https://doi.org/10.1029/2012JA017515

Ni, B., Cao, X., Zou, Z., Zhou, C., Gu, X., Bortnik, J., et al. (2015). Resonant scattering of outer zone relativistic electrons by multiband EMIC waves and resultant electron loss time scales. *Journal of Geophysical Research: Space Physics*, *120*(9), 7357–7373. https://doi.org/10.1002/2015JA021466

Saikin, A. A., Zhang, J.-C., Allen, R. C., Smith, C. W., Kistler, L. M., Spence, H. E., et al. (2015). The occurrence and wave properties of H+-He+-and O+-band EMIC waves observed by the Van Allen Probes. *Journal of Geophysical Research: Space Physics*, *120*(9), 7477–7492. https://doi.org/10.1002/2015JA021358

Shue, J.-H., Song, P., Russell, C. T., Steinberg, J. T., Chao, J. K., Zastenker, G., et al. (1998). Magnetopause location under extreme solar wind conditions. *Journal of Geophysical Research*, *103*(A8), 17691–17700. https://doi.org/10.1029/98JA01103

Thorne, R. M., & Horne, R. B. (1994). Energy transfer between energetic ring current H+ and O+ by electromagnetic ion cyclotron waves. *Journal of Geophysical Research*, *99*(A9), 17275–17282. https://doi.org/10.1029/94JA01007

Tsyganenko, N. A., & Sitnov, M. I. (2005). Modeling the dynamics of the inner magnetosphere during strong geomagnetic storms. *Journal of Geophysical Research*, *110*(A3), A03208. https://doi.org/10.1029/2004JA010798

Usanova, M. E., Drozdov, A., Orlova, K., Mann, I. R., Shprits, Y., Robertson, M. T., et al. (2014). Effect of EMIC waves on relativistic and ultrarelativistic electron populations: Ground based andVanAllenProbesobservations. *Geophysical Research Letters*, *41*(5), 1375–1381. https://doi.org/10.1002/2013GL059024

Usanova, M. E., Mann, I. R., Bortnik, J., Shao, L., & Angelopoulos, V. (2012). THEMIS observations of electromagnetic ion cyclotron wave occurrence: Dependence onAE, SYM-H, and solar wind dynamic pressure. *Journal of Geophysical Research*, *117*(A10), A10218. https://doi.org/10.1029/2012JA018049

Wang, D., Yuan, Z., Deng, X., Zhou, M., Huang, S., Li, M., et al. (2014). Compression-related EMIC waves drive relativistic electron precipitation. *Science China Technological Sciences*, *57*(12), 2418–2425. https://doi.org/10.1007/s11431-014-5701-3

Xu, Z. H., Hartinger, M. D., Clauer, R., Weimer, D., Deshpande, K., Kim, H., et al. (2019). Newly established autonomous adaptive low-power instrument platform (AAL-PIP) chain on East Antarctic Plateau and operation. *Adv Polar Sci*, *30*(4), 362–374. https://doi.org/10.13679/j.advps.2019.0028

Xue, Z., Yuan, Z., & Yu, X. (2021). Prompt emergence and disappearance of EMIC waves driven by the sequentially enhanced solar wind dynamic pressure. *Geophysical Research Letters*, *47*(2), e2020GL091479. https://doi.org/10.1029/2020GL091479

Xue, Z., Yuan, Z., Yu, X., Deng, D., Huang, Z., & Raita, T. (2022). EMIC waves observed throughout the inner magnetosphere driven by abrupt enhancement of the solar wind pressure. *Geophysical Research Letters*, *49*(9), e2022GL098954. https://doi.org/10.1029/2022GL098954

Yu, X., & Yuan, Z. (2019). Saturation characteristics of parallel EMIC waves in the inner magnetosphere. *Geophysical Research Letters*, *46*(14), 7902–7910. https://doi.org/10.1029/2019GL083630

Yu, X., Yuan, Z., Huang, S., Wang, D., Li, H., Qiao, Z., & Yao, F. (2017). EMIC waves covering wide L shells: MMS and Van Allen Probes observations. *Journal of Geophysical Research*, *122*(7), 7387–7395. https://doi.org/10.1002/2017JA023982

Yuan, Z., Xiong, Y., Li, H., Huang, S., Qiao, Z., Wang, Z., et al. (2014). Influence of precipitating energetic ions caused by EMIC waves on the subauroral ionospheric *E* region during a geomagnetic storm. *Journal of Geophysical Research*, *119*(10), 8462–8471. https://doi.org/10.1002/2014JA020303

Yuan, Z., Yu, X., Wang, D., Huang, S., Li, H., Yu, T., et al. (2016). In situ evidence of the modification of the parallel propagation of EMIC waves by heated He+ ions. *Journal of Geophysical Research*, *121*(7), 6711–6717. https://doi.org/10.1002/2016JA022573

Zhang, X.-J., Mourenas, D., Artemyev, A. V., Angelopoulos, V., & Thorne, R. M. (2017). Contemporaneous EMIC and whistler mode waves: Observations and consequences for MeV electron loss. *Geophysical Research Letters*, *44*(16), 8113–8121. https://doi.org/10.1002/2017GL073886